Inhibition of type III radio emissions due to the interaction between two electron beams: Observations and simulations

C Briand, Pierre Henri, S Hoang

AGU PUBLICATIONS

JGR

Journal of Geophysical Research: Space Physics

RESEARCH ARTICLE

10.1002/2013JA019688

Key Points:
- A solar radio emission depletion is observed
- The intersection of two electron beams modifies the physical processes
- Bump-on-tail is reduced, limiting the level of Langmuir waves

Correspondence to:
C. Briand,
carine.briand@obspm.fr

Citation:
Briand, C., P. Henri, and S. Hoang (2014), Inhibition of type III radio emissions due to the interaction between two electron beams: Observations and simulations, *J. Geophys. Res. Space Physics*, *119*, 2365–2378, doi:10.1002/2013JA019688.

Received 22 DEC 2013
Accepted 7 MAR 2014
Accepted article online 13 MAR 2014
Published online 2 APR 2014

Inhibition of type III radio emissions due to the interaction between two electron beams: Observations and simulations

C. Briand[1], P. Henri[2,3], and S. Hoang[1]

[1]LESIA, Observatoire de Paris, CNRS, UPMC, Université Paris Diderot, Meudon, France, [2]Observatoire de la Côte d'Azur, CNRS, Université de Nice Sophia Antipolis, Nice, France, [3]LPC2E, CNRS, Université dOrléans, OSUC, Orléans, France

Abstract We report the peculiar interaction of two type III bursts observed in the solar wind. As electron beams propagating on the same magnetic field lines cross, a spectacular depletion of the type III radio emission is observed. We combine observations from the WAVES experiment on board the STEREO mission together with kinetic plasma simulations to study the extinction of type III radio emission resulting from the interaction between two electron beams. The remote observations enable to follow the electron beams in the interplanetary medium and show that the level of radiated radio waves is recovered after the beam crossing. The in situ observations of beam-driven Langmuir waves give evidence for Langmuir decay. The density fluctuations are extracted from in situ observations. The velocity of the beams is independently evaluated from in situ observations of decaying Langmuir waves and remote radio observations. The kinetic simulations show that the level of beam-driven Langmuir waves is reduced as the two beams cross. We show that the slow beam induced a strong reduction of the quasilinear relaxation of the fast beam, limiting the amplitude of the generated Langmuir waves. Moreover, in the case of two electron beams, the lack of Langmuir wave coherence reduces the efficiency of the Langmuir parametric decay. We thus conclude that the observed depletion of the type III radio emission is independent of the radio emission mechanism, as long as it depends on the Langmuir amplitude and coherence.

1. Introduction

Type III bursts are among the most intense solar radio emissions. These emissions arise at the plasma frequency or its first harmonic and show a characteristic fast downward drift in frequency with time. Numerous works have been devoted to study the physical processes at their origin, and in particular the conversion process from electrostatic to electromagnetic radiations. The most admitted scenario of the type III emission is as follows. Solar flares eject fast electron beams that propagate along the open solar magnetic field lines in the interplanetary medium. The streaming of these electrons provide the necessary free energy to destabilize the plasma (through the bump-on-tail instability) and generate Langmuir waves. These waves are then converted to electromagnetic waves at the local plasma frequency or its harmonic. As the density decreases with the distance to the Sun, the plasma frequency decreases, and the type III exhibits their characteristic time-frequency drift. Several wave conversion processes have been discussed from linear mode conversion in inhomogeneous density profiles [*Field*, 1956; *Kim et al.*, 2008; *Schleyer et al.*, 2013] to nonlinear processes including nonlinear beam instability [*Yoon*, 1995], wave coupling (electrostatic parametric decay [*Cairns*, 1987b; *Henri et al.*, 2009], or electromagnetic coupling [*Cairns*, 1987a]).

Recently, *Henri et al.* [2009] have provided strong observational evidence in favor of the electrostatic parametric decay. This is a two-step process that yields to an electromagnetic wave at twice the plasma frequency. When the amplitude of the Langmuir wave is large enough, the wave decays into a daughter Langmuir wave L' and an ion acoustic wave IAW. In the second step, two Langmuir waves couple to generate the electromagnetic wave:

$$L \rightarrow L' + \mathrm{IAW} \quad L + L' \rightarrow T_{2f_p} \tag{1}$$

To complete this observational work, *Henri et al.* [2010] performed Vlasov simulations. They first provided a new estimate of the amplitude threshold for the parametric decay to occur in the realistic case of wave packets (i.e., not only for monochromatic waves), and they show that the observed wave amplitudes fulfill the conditions of decay.

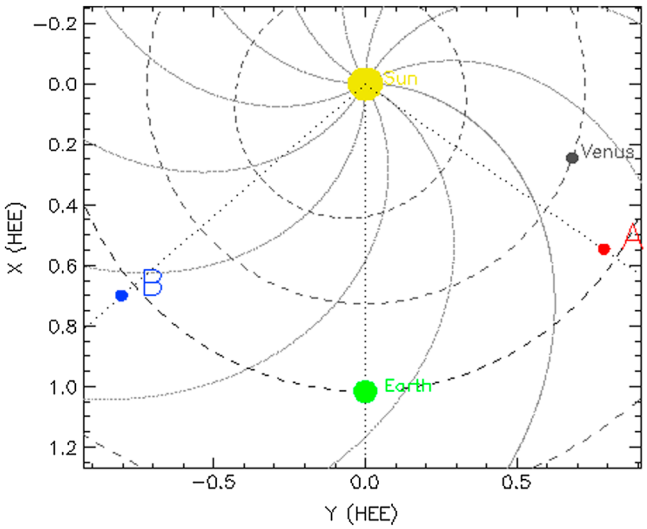

Figure 1. Location of the two STEREO spacecraft relative to the Earth at the time of the observation. Earth, Venus, and Mercury orbits are displayed together with the Parker spiral. From the STEREO Web page.

In the present paper, we provide another indirect evidence in favor of the nonlinear process from observations and Vlasov simulations. Since the type III emission is at the fundamental of the plasma frequency, electromagnetic coupling is favored in the present case either through an electromagnetic decay:

$$L \rightarrow T_{f_p} + \mathrm{IAW} \tag{2}$$

or through a coalescence process:

$$L + \mathrm{IAW} \rightarrow T_{f_p} \tag{3}$$

The new aspect of these observations is the strong decrease of the intensity of the type III emission. We interpret it as the reduction of the Langmuir wave emissions due to the interaction of two electron beams ejected at different time in the interplanetary medium while following the same open magnetic field line. As will be shown, two distinct beams of electrons with different speeds generate the recorded type III emissions. The first emitted beam is composed of electrons slightly slower than those of the second beam, injected later from the Sun in the interplanetary medium. As the fast beam catches up with slower one, a striking lack of the radio flux nearby the burst leading edge can be observed. When the faster beam exceeded the slow one, the two type III radio emission components recover their standard radio flux. The goal of this paper is thus to explain the inhibition of the electromagnetic emission through 1D-1V Vlasov-Poisson simulations. Indeed, following the idea that Langmuir waves are the first step of a wave coupling that leads to the electromagnetic radiation, we plan to estimate how this coupling can be broken or reduced.

The paper is organized as follows. The section 2 presents the conditions of observation. The section 3 details the analysis from the remote and in situ observations to deduce the parameters that serve to constrain the simulations presented in section 4.

2. Observations

The STEREO mission is composed of two nearly identical spacecraft, one orbiting ahead of the Earth (STEREO-A) and the other behind (STEREO-B). The observations were performed by the radio instrument WAVES [*Bougeret et al.*, 2008; *Bale et al.*, 2008]. The High/Low Frequency Receiver (HFR/LFR) continuously records electric field in the range 20 kHz–16 MHz, and the Time Domain Sampler (TDS) mode records high time resolution, electric waveforms in the range 0.1 to 60 kHz. The analysis of the waveforms also requires several other parameters of the solar wind. In particular, the magnetic field and the solar wind parameters are obtained, respectively, from the In-situ Measurements of Particles and CME Transients (IMPACT) [*Luhmann et al.*, 2008] and Plasma and Suprathermal Ion Composition (PLASTIC) [*Galvin et al.*, 2008] instruments on board STEREO. Finally, the images at 171, 195, and 294 Å obtained by Sun Earth Connection

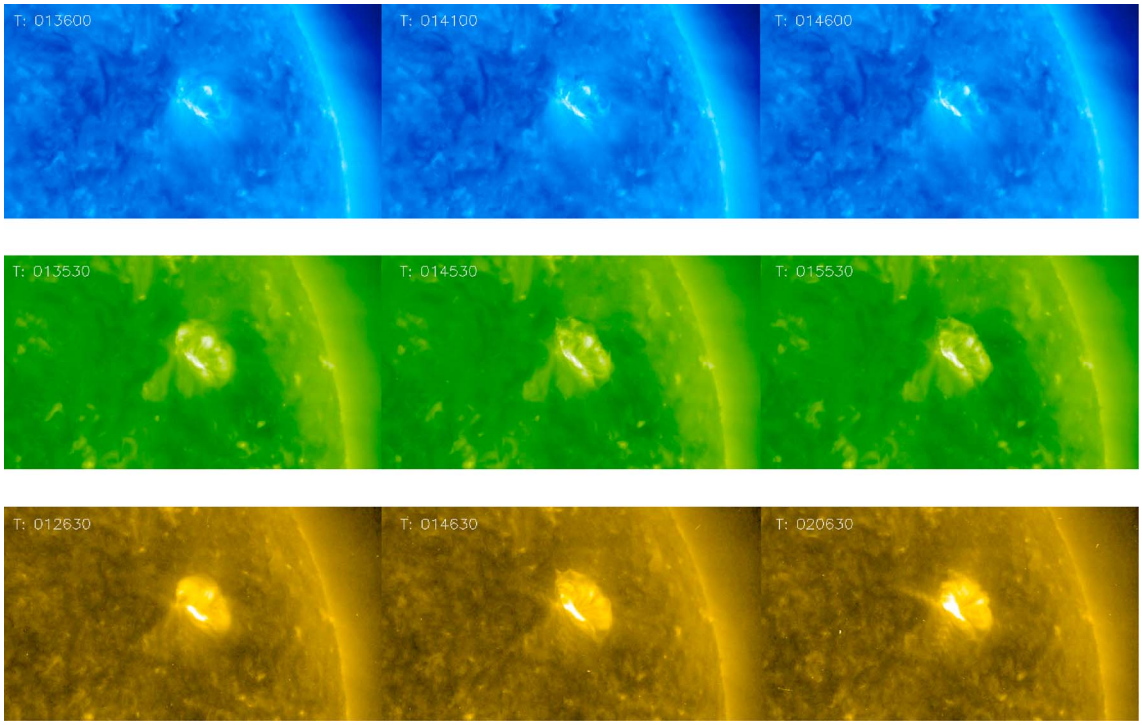

Figure 2. Close view of the unique active region responsible for the type III emission, as observed by SECCHI instrument. (from top to bottom) 171 Å, 195 Å, and 294 Å. The time of each image is indicated (in universal time) and increases from left to right.

Coronal and Heliospheric Investigation (SECCHI) are used to identify the active region at the origin of the radio event [*Howard et al.*, 2008].

The observations were performed on 18 July 2009 by STEREO-A. At that date, STEREO-A was located in the ecliptic plane, at 0.958 AU from the Sun and 55.3° to the west of the Earth (see Figure 1). While this emission was also observed by the radio receiver of the Wind/WAVES instrument (not shown) located ahead of the Earth, it had no significant counterpart on STEREO-B located 49° east of the Earth.

The inspection of the SECCHI images (Figure 2) reveals that only a small active region, located at N28°W120°, was present on that day, facing ST-A. Between 01:30 and 02:00 UT (corresponding to the deduced onset time of the radio emission, see below), we observe a lift off of plasma material from this region. This confirms our identification of this region as the unique source of the electron beams. About 1 h later, the brightness in 195 and 294 Å increases.

2.1. Remote Sensing Observations

Figure 3 displays the radio spectrogram from 01:00 to 04:30 UT. At high frequency, the burst exhibits two main components. The first emission, labeled ${F_A}^1$, starts at $t^1_{\mathrm{HF}} \approx$ 01:38 UT ($t = 1.6357$ on Figure 3) while the second one, labeled ${F_A}^2$, starts at $t^2_{\mathrm{HF}} \approx$ 01:47 UT ($t = 1.79$). At low frequency, intense Langmuir waves (LW) are observed, starting at $t^1_{\mathrm{LW}} \approx$ 02:42 UT ($t = 2.7046$) for the first group, labeled LW_1, and $t^2_{\mathrm{LW}} \approx$ 03:17 UT ($t = 3.2850$) for the second compact group LW_2. The presence of such waves reveals the passage of electron beams by the probe location.

The method to determine the mode of emission (fundamental or harmonic) and the velocity of the electron beams has been intensively described in *Dulk et al.* [1987] and *Hoang et al.* [1994, 2007]. We just summarize the main ideas here and develop the results.

The type III emissions are emitted at the local plasma frequency f_p (for the fundamental, with f_p (kHz) $= 8.98 \times n_e^{1/2}$ when the density is expressed in cm^{-3}) or twice this frequency (for the harmonic). At the heliocentric distances covered by our frequency range, the electron density n_e varies as r^{-2}, r being the distance to the Sun (in astronomical unit). A diagram displaying the time variation of the intensity as a function of the inverse of the frequency ($1/f - t$ diagram) thus shows the variation of the emission with the distance to the

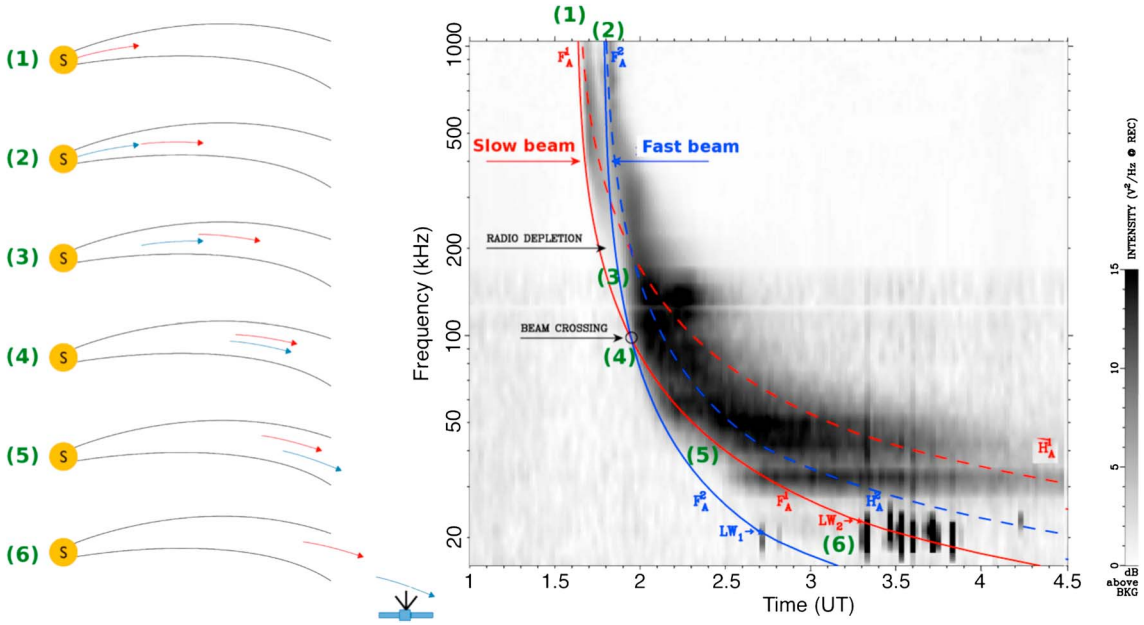

Figure 3. (left) Schematic view of the two electron beams' positions corresponding to the radio observations. The numbers 1–6 are used to define several moments of the beam propagation. (right) Radio spectrogram observed by STEREO-A on 18 July 2009 from 01:00 to 05:30 UT in the 15–1000 kHz range. The intensity relative to background is plotted as a function of time (hour of day) and frequency (kHz) and coded by a gray scale in units of decibel above background. The solid lines, labeled $F_A{}^1$ (red) and $F_A{}^2$ (blue), are the traces of the predicted onset times for the type III electrons producing the fundamental (F) radiation while the dashed lines (H) stand for the respective predicted onset time of the harmonic radiation. Both traces, $F_A{}^1$ (slow stream) and $F_A{}^2$ (fast stream), clearly delineate the leading edges of the two burst components at high frequency before they intersect at about 1.93 UT and 100 kHz (beam crossing).

Sun [*Dulk et al.*, 1987; *Hoang et al.*, 1994, 2007]. The linear fit of $1/f$ versus the emission onset time at highest frequencies (i.e., near the Sun where the spiral is quasiradial) yields for the first burst component, labeled F_A^1 in Figure 3, a beam speed slower than that of the second component F_A^2 (see details in section 3). This implies that the first and slow burst F_A^1 is to be associated with the second group of Langmuir waves LW_2, and the second and fast burst F_A^2 with the first group LW_1. From the knowledge of the mean beam speed along the spiral and assuming the plasma frequency f_p distribution in $1/r$ along the spiral, the onset times at the fundamental F and harmonic H as a function of frequency can be predicted for each burst component, after correction for the light flight time from the type III emission source to spacecraft.

The onset times are plotted in Figure 3 for the first component $F_A{}^1$ corresponding to the slow stream (red color) and for the second component $F_A{}^2$ corresponding to the fast stream (blue color). A striking lack of the radio flux nearby the burst leading edge of the two beams can be observed at the crossing of the two beams, from ~200 kHz down to ~100 kHz (at about $t = 1.93$). Below the beam crossing frequency at 100 kHz, the radio emission appears again immediately after the leading edge of the fast stream and thus overwhelms that of the slow stream.

2.2. In Situ Observations

As the electron beams cross the STEREO-A spacecraft between 02:42 and 04:04 UT (step (6) in Figure 3), beam-driven Langmuir waves are recorded by the Time Domain Sampler (TDS) of the S/WAVES experiment. A total of 45 waveforms have been recorded. Except for the first event at 02:42 UT, they all correspond to the compact group of Langmuir waves LW_2 previously discussed which is linked to the slow beam.

Originally recorded in the antenna reference frame, the waveforms are studied in a more physical reference frame $(\vec{e}_{\parallel}, \vec{e}_{\perp 1}, \vec{e}_{\perp 2})$ where $\vec{e}_{\parallel}$ is along $\vec{B}$, $\vec{e}_{\perp 1}$ is along $\vec{V}_{SW} \times \vec{B}$, where $\vec{V}_{SW}$ is the solar wind velocity, and $\vec{e}_{\perp 2}$ completes the orthonormal trihedral. An example of such waveform is shown in Figure 4.

The first event at 02:42 intersects the predicted onset time emission of the fast beam (blue, full line F_A^2 of Figure 3). The envelop of the waveform has a soliton shape meaning that the emission is very localized. The polarization is elliptic in the plane $(\vec{e}_x, \vec{e}_y)$. The spectrum shows a double peak with a large power at 20.10 kHz. No low-frequency counterpart is observed. The 44 remaining events correspond to the compact group of Langmuir waves observed between 03:03 and 04:04 UT. Among these events, 42 show a

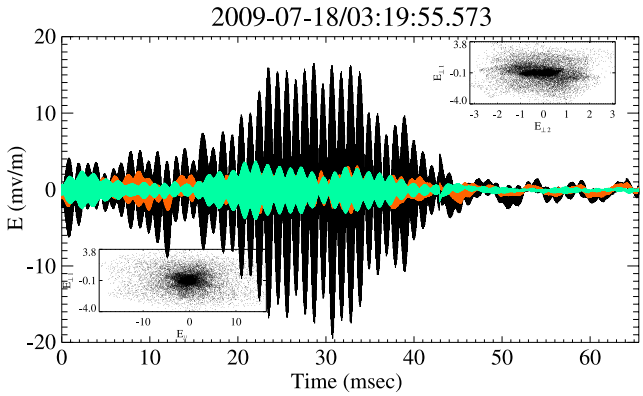

Figure 4. An event of the compact group of Langmuir waves corresponding to the slow beam. The three components of the electric field are displayed. In black $\vec{e}_{\parallel}$, in red $\vec{e}_{\perp 1}$, and in green $\vec{e}_{\perp 2}$. The enclosed figures display the polarization in the plane $(\vec{e}_{\parallel},\vec{e}_{\perp 1})$ (bottom left) and in the plane $(\vec{e}_{\perp 2},\vec{e}_{\perp 1})$ (top right).

double-peak structure around the plasma frequency (Figure 5) with a broadband frequency of about 0.3 kHz. When the intensity of the electric field is high enough (typically greater than 25 mV/m), a low frequency peak ($\leq$ 1 kHz) appears. Its frequency then equals the separation between the two Langmuir wave peaks. Among the 44 recorded events, 19 present a clear low-frequency signature. Note that the absence of such signature does not necessarily mean that the Langmuir decay did not proceed. Such lack could result from a stronger damping of the ion acoustic waves (by a local increase of the ion temperature, for example). It can also indicate that the coalescence process is also at play.

3. Beam Characteristics

The beam velocity to be introduced in the simulation is deduced from the observations, first from the electromagnetic radiation then from the 44 events of in situ Langmuir wave measurements corresponding to the slow beam.

3.1. Beam Velocity

From the r^{-2} radial variation of the electron density and the relation between plasma frequency and density, we obtain

$$B = \frac{\mathrm{d}(1/f)}{\mathrm{d}t} = \frac{V_b}{a(f_p r)_0}, \tag{4}$$

where a is the radiation mode (equals to 1 for fundamental and 2 for harmonic), $V_b = \mathrm{d}r/\mathrm{d}t$ is the electron beam speed, $(f_p r)_0$ can be fixed by the knowledge of f_{p0} at a given heliocentric distance r_0, e.g., at the spacecraft. In the present case, a linear fit of $1/f$ versus the emission onset time for each burst component

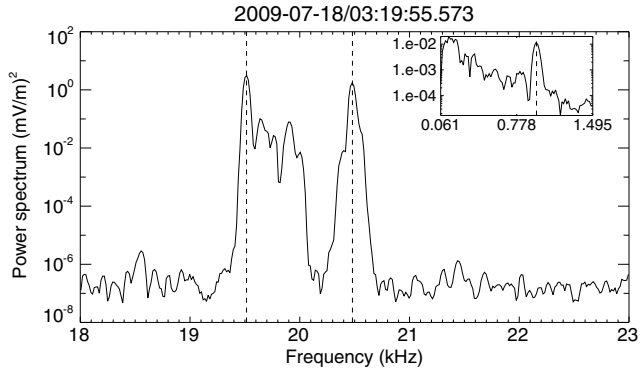

Figure 5. Spectrum of the parallel component of the event presented in Figure 4. The enclosed figure displays the spectrum at low frequency. The vertical dashed lines show the two Langmuir peak frequencies and the expected location of the low-frequency signal.

Table 1. Plasma Parameters Obtained or Deduced From the In Situ Measurements[a]

Event #	Time hh:mm:sec	f_p (kHz)	f_{IA} (kHz)	V_{SW} (km s^{-1})	θ (deg)	V_b (c)	E_{max} (mV/m)
5	03:07:01	20.67	0.58	531	53.0	0.08	37
7	03:07:03	20.83	0.51	531	53.7	0.09	23
8	03:07:05	20.80	0.67	531	52.8	0.07	41
9	03:07:06	20.82	0.53	531	52.8	0.08	32
15	03:10:07	20.65	0.54	525	46.1	0.09	59
16	03:10:09	20.51	0.77	517	48.7	0.06	25
18	03:15:17	21.24	0.79	501	39.9	0.07	23
22	03:15:22	21.28	0.67	501	39.9	0.08	27
23	03:19:55	20.00	0.98	507	30.1	0.06	17
25	03:20:01	20.04	0.92	507	30.4	0.06	37
26	03:20:03	20.11	0.89	507	30.5	0.07	11
28	03:20:26	20.08	0.70	501	31.4	0.08	22
29	03:20:40	20.40	0.84	502	28.6	0.07	16
30	03:20:51	20.12	0.83	502	29.3	0.07	25
34	03:29:41	19.63	0.89	494	40.73	0.06	29
35	03:32:26	20.18	0.96	514	29.35	0.06	37
36	03:32:27	20.37	0.59	514	29.43	0.10	53
41	03:50:47	19.70	0.86	521	45.7	0.05	67
42	03:50:48	19.71	0.91	521	45.8	0.05	57

[a]From left to right: event number, time of the Langmuir event, plasma and ion acoustic wave frequency, solar wind speed, and the angle between the solar wind and the magnetic field. The two last columns give the estimate of the beam velocity (from equation (7)) and the maximum value of the electric field.

was performed between 1075 and 325 kHz. We obtained a slope of $B_1 = 0.036 \pm 10^{-3}$ kHz^{-1} h^{-1} for the first component ${F_A}^1$ and $B_2 = 0.05350 \pm 8.10^{-5}$ kHz^{-1} h^{-1} for the second component ${F_A}^2$. At the location of the spacecraft ($r = 0.958$ AU), the observed plasma frequency is about 20 kHz (see also Table 1), leading to $V_b^1 = 0.096 \pm 0.007c$ for the first beam and $V_b^2 = 0.142 \pm 0.007c$. A first slow electron beam has thus been ejected from the Sun followed by a second, faster one.

Another way to estimate the beam speed is to compute the travel length of the electrons along the Archimedean spiral of the open magnetic field line that connect the Sun to the spacecraft. In the ecliptic plane, the Archimedean (Parker) spiral is written as [*Tautz et al.*, 2011]

$$\frac{r}{b} - 1 - \ln\left(\frac{r}{b}\right) = \frac{v_{SW}}{\Omega_\odot \times b}(\phi - \phi_0) \tag{5}$$

with $b = 46 \times 10^{-3}$ AU the distance to the Sun where the field line corotate with the Sun's surface (i.e., the distance above which the velocity can be considered as constant), $\Omega_\odot = 2.6 \times 10^{-6}$ rad s^{-1} the Sun rotation rate, v_{SW} the radial solar wind velocity, r the distance to the Sun, ϕ the heliocentric longitude at the distance r, and ϕ_0 the heliocentric longitude of the foot point of the magnetic field line. The length of the spiral arc is thus given by *Tautz et al.* [2011]

$$L(r) = \frac{r-b}{2}\frac{\sqrt{(r-b)^2 + \zeta^2}}{\zeta} + \frac{\zeta}{2}\mathrm{Arsinh}\left(\frac{r-b}{\zeta}\right) \tag{6}$$

where $\zeta = v_{SW}/\Omega_\odot \approx 1.33$ AU. Assuming that the two beams have followed the same spiral arc ($L = 1.05 \pm 0.02$ AU with a solar wind speed of $v_{SW} = 520 \pm 10$ km s^{-1}), their velocity is deduced from the difference of flight time: $t_{HF}^1 = 01{:}38$ UT and first detected at the spacecraft at $t_{LW}^1 = 03{:}17$ UT, while the second beam is ejected at $t_{HF}^2 = 01{:}47$ UT and detected at $t_{LW}^2 = 02{:}42$ UT at the spacecraft. This leads to $V_b^1 = 0.09c \pm 0.03$ and $V_b^2 = 0.16 \pm 0.04c$. These mean velocities confirm the sketch of beam emission deduced from the slope

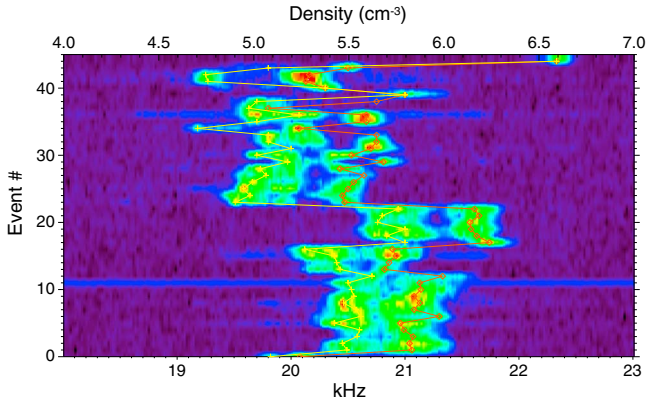

Figure 6. Spectrum around the plasma frequency for all the events of the compact group. The ordinate axis displays the event number, an indication of time (but the events are not regularly observed in time). The red (yellow) line displays the location of the upper (lower) Langmuir peak. The upper abscissa scales the electron density corresponding to the frequencies of the lower axis.

of the $(t - 1/f)$ diagram. It also confirms that the two beams follow the same spiral arc, as expected since only one active region is observed on the Sun (Figure 2).

The velocity of the electron beam V_b can also be estimated from the Langmuir waves. Indeed, the Langmuir decay conserves the energy and the moment. This allows to deduce the relation between the frequency of the waves and the velocity of the electron beam [*Cairns and Robinson*, 1992; *Hospodarsky and Gurnett*, 1995]:

$$V_b \approx \frac{2 f_p V_{SW} \mid \cos(\theta) \mid}{f_{IA}} \tag{7}$$

where f_{IA} is the frequency of the ion acoustic wave, f_p the frequency of the Langmuir wave, V_{SW} the velocity of the solar wind, and θ the angle between the magnetic field and solar wind. This equation is correct in case of electrostatic decay (equation (1)). It is not valid in case of coalescence or electromagnetic decay. However, we will see that the electron beam values obtained from equation (7) are consistent with the estimation of the former paragraphs. We discuss this in the conclusions. The plasma frequency entering in equation (7) is set to the mean value of the two Langmuir peaks, since the two components are supposed to be equally Doppler shifted in opposite direction. Table 1 presents the parameters of the observation and the estimate of the beam velocity for all events where the low frequency wave is clearly observed. They are compatible with the value of the slow speed beam deduced from the electromagnetic radiation.

Equation (7) also shows that the frequency of the ion acoustic wave must increase with time, as the beam speed decreases. We have checked (not shown) that this time evolution is indeed observed, with a mean drift of 455 Hz h^{-1}.

3.2. Main Plasma Density Fluctuations

If we neglect the correction due to thermal effect, the frequency of the Langmuir waves is proportional to the square root of the core electron density. Figure 6 displays the time evolution of the frequency (thus the density). The variations of the electron density is about 20% during the observing time of the Langmuir waves.

The Langmuir ponderomotive effect couples the electron and ion dynamics. Using the STEREO spacecraft floating potential fluctuations, it is possible to estimate the density fluctuations $\delta n/n_{max}$ [*Henri et al.*, 2011]. Figure 7 shows that the nonlinear effects start playing an important role for an electric to thermal energy ratio larger than about 10^{-4}: the events are then located along the line of saturation $\delta n/n_{max} = W_L$. Note that the same conclusion was obtained in the aforementioned paper from the analysis of data from the free (i.e., not connected to Earth) solar wind and terrestrial electron foreshock. This proves the fundamental aspect of the nonlinear process, independently of the mode of excitation of the electromagnetic waves.

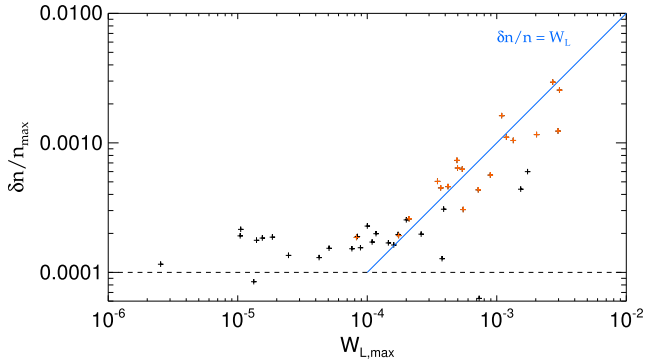

Figure 7. Density fluctuation ($\delta n/n_{max}$) as a function of the maximum Langmuir wave energy $W_{L,max}$. Red points correspond to the event of Table 1. The blue line displays the saturation level of the parametric decay, i.e., the location where ($\delta n/n_{max}$) = W_L. The horizontal dashed line indicates the 3σ detection level of S/WAVES.

4. Simulations

So far, we have reported remote radio observations of two interacting type III bursts and in situ observations of decaying beam-driven Langmuir waves as the type III associated electron beam crosses the STEREO-A spacecraft. In this section, we analyze the origin of the radio extinction, corresponding to steps (3) and (4) in Figure 3. In this purpose, we make use of kinetic simulations to explore the properties of the beam-plasma interactions and the eventual Langmuir decay as the two electron beams intersect.

A kinetic electromagnetic simulation to model the type III radio emissions is still out of reach of current computers. In order to understand the physical mechanisms at the origin of the decrease of the electromagnetic emission at the beam crossing, we make use of a kinetic electrostatic model instead, using the efficiency of the beam-driven Langmuir waves generation and subsequent nonlinear electrostatic decay as an estimation of the efficiency of the radio emission mechanism.

4.1. Model

The Vlasov-Poisson system of equations is solved for the electron and ion distribution functions, $f_e(x, v, t)$ and $f_i(x, u, t)$, with the numerical scheme described in *Mangeney et al.* [2002]. A 1D-1V configuration is considered in this study. The equations are normalized using the following characteristic electron quantities: the charge e, the electron mass m_e, the electron density n_e, the plasma (angular) frequency $\omega_{pe} = \sqrt{4\pi n_e e^2/m_e}$, the Debye length $\lambda_D = \sqrt{T_e/4\pi n_e e^2}$, the electron thermal velocity $v_{th,e} = \lambda_D \omega_{pe} = \sqrt{T_e/m_e}$, and an electric field $\bar{E} = m_e v_{th,e} \omega_{pe}/e$. Then, the dimensionless equations for each species read

$$\frac{\partial f_e}{\partial t} + v\frac{\partial f_e}{\partial x} - E\frac{\partial f_e}{\partial v} = 0 \tag{8}$$

$$\frac{\partial f_i}{\partial t} + u\frac{\partial f_i}{\partial x} + \frac{E}{\mu}\frac{\partial f_i}{\partial u} = 0 \tag{9}$$

$$\frac{\partial^2 \phi}{\partial x^2} = \int f_e \mathrm{d}v - \int f_i \mathrm{d}u \; ; E = -\frac{\partial \phi}{\partial x} \tag{10}$$

where v (resp. u) is the electron (resp. ion) velocity. Here $\mu = m_i/m_e = 1836$ is the ion-to-electron mass ratio. The self-consistent electric potential (ϕ) and electric field E are generated by the plasma charge density fluctuations according to Poisson equation (equation (10)). The electron (resp. ion) distribution function is discretized in space for $0 \leq x < L_x$, with $L_x = 10,000\ \lambda_D$ the total box length, with a resolution $\mathrm{d}x = \lambda_D$. The electron velocity grid ranges over $-20\ v_{th,e} \leq v \leq +20\ v_{th,e}$, with a resolution of $\mathrm{d}v = 0.1\ v_{th,e}$. The ion velocity grid ranges over $-5\ u_{th,i} \leq u \leq +5\ u_{th,i}$, with a resolution of $du = 0.04\ u_{th,i}$, where $u_{th,i}$ is the ion thermal velocity. Finally, periodic boundary conditions are used in the spatial direction. The beams length (estimated from the duration of the Langmuir activity and the respective beam velocities) is much larger (≈15–30 × 10^6 km) than the Langmuir wavelength (≈0.25 km at the beam crossing position) and Langmuir wave packets (≈5 km at the beam crossing position). Thus, periodic (i.e., infinite beams) condition is reasonable.

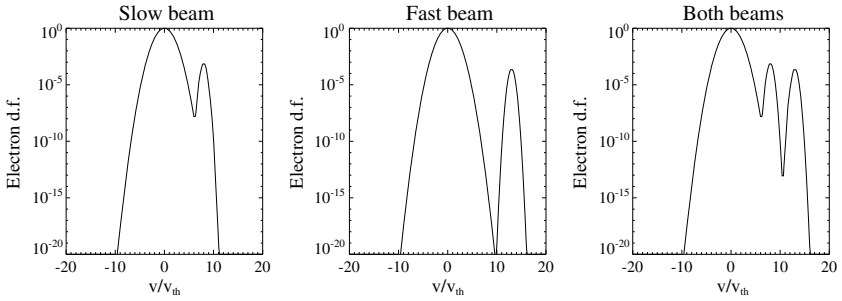

Figure 8. Initial electron distribution functions in velocity space: (from left to right) the slow beam only, the fast beam only, and both beams are present in the simulation box.

In all the runs, the following initial conditions have been chosen: ion distribution functions are initially Maxwellian with respect to velocity, while electron distribution functions are composed of a Maxwellian core and one or two Maxwellian beams; a random noise is added to the homogeneous density to seed the generation of beam-driven Langmuir waves:

$$f_e(x,v) = \left(f_e^{\text{core}}(v) + f_e^{b,\text{slow}}(v) + f_e^{b,\text{fast}}(v)\right) \times \left(1 + \epsilon \sum_k \cos\left(kx + \psi_k\right)\right) \tag{11}$$

where

$$f_e^{\text{core}}(v) = \left(1 - n^{b,\text{slow}} - n^{b,\text{fast}}\right) \frac{\exp\left(-\frac{v^2}{2v_c^2}\right)}{\sqrt{2\pi}} \tag{12}$$

$$f_e^{b,\text{slow}}(v) = \frac{1}{\sqrt{2\pi}} \frac{n^{b,\text{slow}}}{v_{b,\text{th}}} \exp\left(-\frac{(v - v_{b,\text{slow}})^2}{2v_{b,\text{th}}^2}\right) \tag{13}$$

$$f_e^{b,\text{fast}}(v) = \frac{1}{\sqrt{2\pi}} \frac{n^{b,\text{fast}}}{v_{b,\text{th}}} \exp\left(-\frac{(v - v_{b,\text{fast}})^2}{2v_{b,\text{th}}^2}\right) \tag{14}$$

and

$$f_i(x,u) = \sqrt{\frac{\Theta}{2\pi\mu}} e^{-\frac{\Theta}{\mu}\frac{u^2}{2}} \times \left(1 + \epsilon' \sum_k \cos\left(kx + \psi_k'\right)\right) \tag{15}$$

with $\mu = m_i/m_e = 1836$ is the ion-to-electron mass ratio, $\Theta = T_i/T_e$ is the ion-to-electron temperature ratio set to $\Theta = 0.1$ in the different runs. ψ_k and ψ_k' are random phases with a uniform distribution. The parameter ϵ (resp. ϵ') is the amplitude of the initial electron (resp. ion) density level of noise. They are chosen so that the development of the instability occurs relatively rapidly, as Vlasov codes have a very low level of numerical noise.

The beams thermal velocity is fixed to $v_{b,\text{th}} = 0.35$. The two beam speed are $v_{b,\text{slow}} = 8$ and $v_{b,\text{fast}} = 13$ for the slow and fast beam, respectively. The beam densities are $n_{b,\text{slow}} = 1.5 \times 10^{-3}$ and $n_{b,\text{fast}} = 5 \times 10^{-4}$ for slow and fast beam, respectively, expressed in units of the core electron density. The parameters are chosen so that the growth rate of beam-driven Langmuir waves generated by the two isolated beams is of the same order. We have performed a series of three different setups: in the first (resp. second) setup, only the slow (resp. fast) beam is present, while in the third run, both the slow and fast beams are launched. Figure 8 shows the initial electron distribution function corresponding to the three setups. In this numerical experiment, the first and second setups are intended to model the generation and evolution of Langmuir waves when the beams are present separately (steps (2), (5), and (6) in Figure 3), while the third run is intended to model the generation and evolution of Langmuir waves as the two electron beams intersect (steps (3) and (4)).

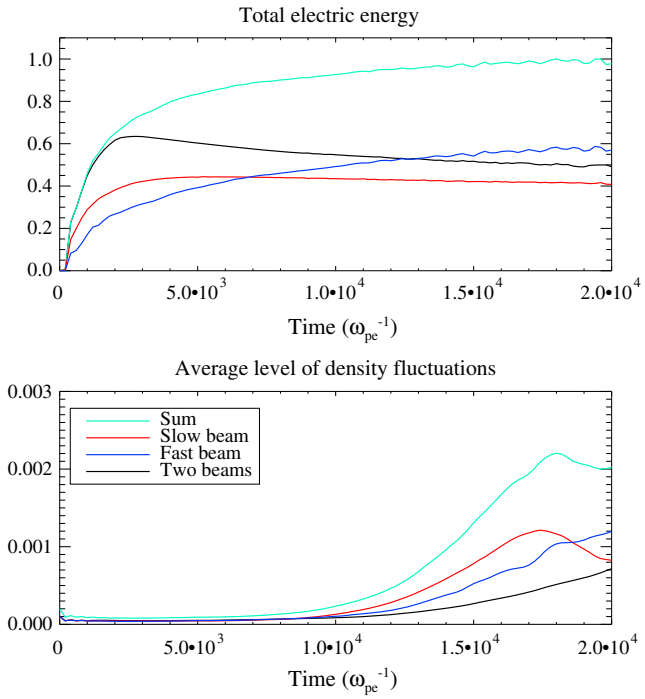

Figure 9. Evolution of the (top) total electric energy and (bottom) average level of density fluctuations when the slow beam only (red), the fast beam only (blue), or both beams (black) are present. The green line shows the sum of the isolated contribution of the two beams. To ease the reading, the electric energy is normalized to the maximum of electric energy corresponding to the sum of the electric energy when the beam is isolated.

4.2. Generation and Evolution of Langmuir Waves as the Two Electron Beams Cross

The slow (resp. fast) electron beam is unstable to the bump-on-tail instability leading to the generation of Langmuir waves with an electric spectrum centered on wave number $k_{L,\mathrm{slow}} = 0.14$ ($k_{L,\mathrm{fast}} = 0.08$). When the energy of the Langmuir waves is high enough, they undergo a three-wave electrostatic decay that generates backscattered daughter Langmuir waves with a wave vector $k_{L',\mathrm{slow}} \simeq 0.12$ ($k_{L',\mathrm{fast}} \simeq 0.07$) and ion acoustic waves with $k_{S,\mathrm{slow}} \simeq 0.26$ ($k_{S,\mathrm{fast}} \simeq 0.15$).

The level of electric energy is used as a proxy for the efficiency of the bump-on-tail instability, while the level of density fluctuations is a proxy for the efficiency of the three-wave coupling process. The evolution of the electric energy and of the level of density fluctuations is shown in Figure 9. After a linear phase of the bump-on-tail instability ($0 < t < 2.10^4$), the level of Langmuir electric energy (Figure 9, top) saturates to a level that is of the same order for the two beams taken isolated (compare the blue and red lines). As the amplitude of the Langmuir waves reaches the parametric decay threshold [*Henri et al.*, 2010], the level of associated density fluctuations grows (Figure 9, bottom). Note that both the level of Langmuir electric energy (Figure 9, top) and the level of density fluctuations (Figure 9, bottom) when the two beams are present (black line) is smaller than what would be expected with independent bump-on-tail instabilities (green line). This proves that the three-wave coupling is less efficient when the two beams are present. The density fluctuation depletion in presence of two beams is a direct consequence of the lower Langmuir electric energy, as the parametric decay threshold depends on the Langmuir amplitude.

We now concentrate on the reason for this electric energy depletion, in particular the influence of the slow beam on the decrease of fast beam-driven Langmuir energy; then we shall discuss the mutual influence of each beam-driven Langmuir wave on the decay of the other.

4.2.1. Decrease of the Fast Beam-Driven Langmuir Energy

The evolution of the electric spectrum is shown in Figure 10 where only the slow beam (top), only the fast beam (middle), or both beams (bottom) are considered. If only one beam is present, the electric spectrum shows first the growth of the beam-driven Langmuir waves (L_1 and L_2), then the growth of the daughter Langmuir wave as the parametric decay proceeds (L_1' and L_2').

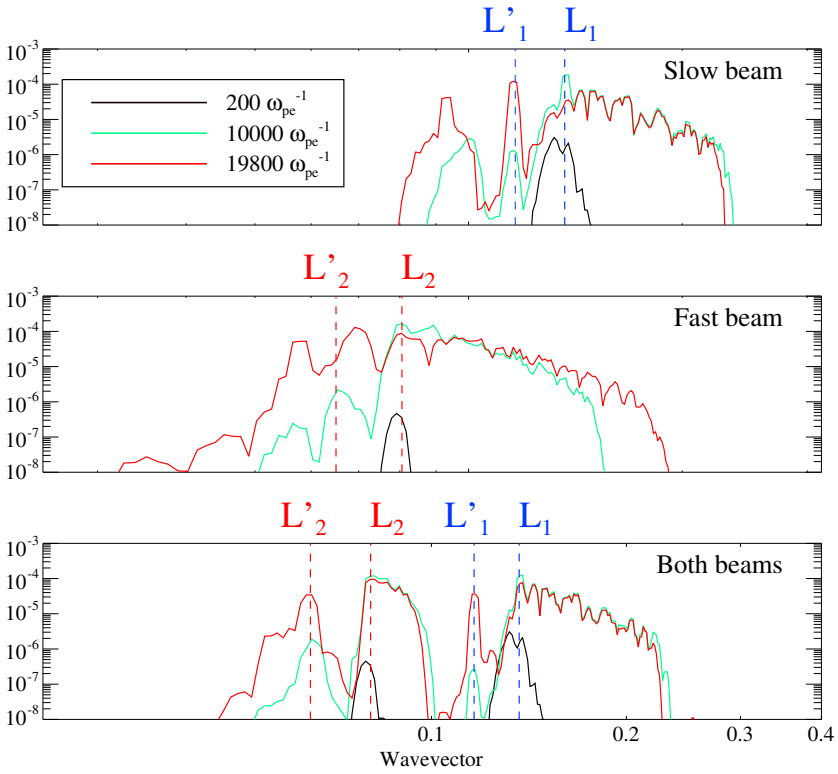

Figure 10. Electric spectrum at successive moments of the simulation. (top) Only the slow beam, (middle) only the fast beam, (bottom) the two beams are present. The different moments are displayed by distinct colors. The time values are indicated in Figure 10, top. The vertical dashed lines show the wavelength of the mother (L) and daughter (L') Langmuir waves corresponding to the decay of the slow (blue) and fast (red) beam-driven Langmuir waves.

Note that the broadening of the beam-driven Langmuir spectrum develops toward larger wave numbers. If only one beam is present, the spectral broadening develops on wave numbers ranging from the linear bump-on-tail wave number (resp. k_{L1} and k_{L2}) to a larger wave number (Figure 10, top and middle). When both beams are present (Figure 10, bottom), the spectral broadening of the slow beam-driven Langmuir waves is identical to what is observed with only the slow beam (Figure 10, top). On the contrary, the spectral broadening of the fast beam-driven Langmuir waves is stopped early, at a wavelength ($\simeq$ 0.015) much smaller than what is observed with the fast beam only (Figure 10, middle).

This spectral broadening is associated to the quasilinear evolution of the electron distribution function, more precisely the broadening of the plateau. As the unstable part of the distribution function (positive velocity slope) is moved toward smaller velocities, resonant Langmuir waves at larger wave numbers develop. This can be understood from the screening of the fast beam by the slow beam in velocity space (Figure 11), which limits the formation of the plateau associated to the fast beam to velocities larger than the initial slow beam velocity. As a consequence, the available free energy to be converted into electric energy is much smaller for the fast beam-driven Langmuir waves in presence of the slow beam. Eventually, the density fluctuations associated to the Langmuir decay are reduced when the Langmuir wave amplitude is smaller. In association to this quasilinear picture that explains the screening of the fast beam by the slow beam, the fast beam electron trapping process is strongly modified in the presence of the slow beam, as the trapped fast electrons access a smaller range of velocities in phase space (not shown here).

The beam densities are assumed as a parameter in the simulation as they are not available from STEREO data. The relative beam density $n_{b,\mathrm{slow}}/n_{b,\mathrm{fast}}$ however plays an important role in the quasilinear relaxation of the fast beam. Indeed, the result presented in Figure 11 would become qualitatively different with $n_{b,\mathrm{slow}}/n_b, \mathrm{fast} \ll 1$, since the quasilinear relaxation of the fast beam would no longer be inhibited at velocities smaller than $v_{b,\mathrm{slow}}$ so that the total available free energy from the fast beam would not differ much in the presence or absence of the slow beam with $n_{b,\mathrm{slow}}/n_b, \mathrm{fast} \ll 1$. This tends to suggest that during the

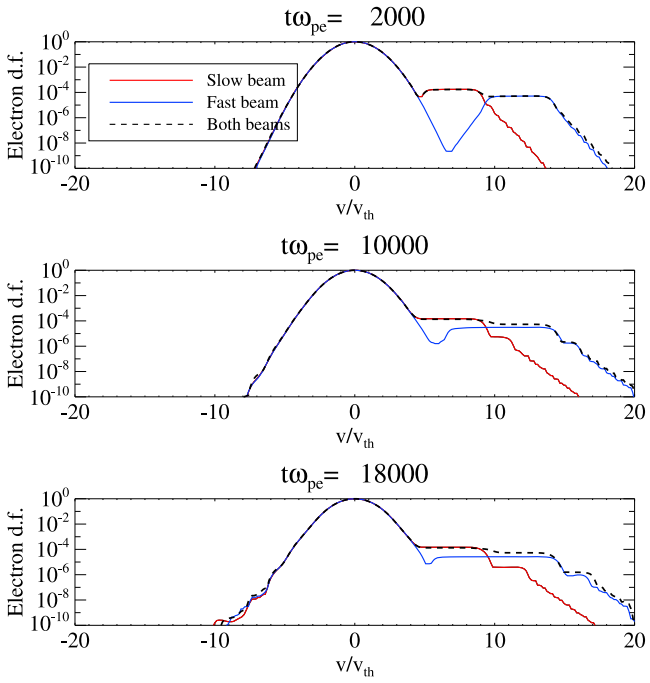

Figure 11. Comparison of the velocity electron distribution functions, averaged on the numerical box, at (from top to bottom) three successive times $\omega_{pe}t = 2 \times 10^3$, 10×10^3 and 18×10^3, when the slow beam only (in full red), the fast beam only (in full blue), or both beams (in black dashed) are considered.

event reported in this paper, the density of the fast beam should not have been much larger than that of the slow beam.

Figure 9 shows that the total electric energy in the presence of both beams is always larger than when the slow beam only is present, but that the corresponding density fluctuation is always smaller than the isolated contributions of the two beams. This indicates that not only the fast beam-driven Langmuir waves are affected by the slow beam, but that another process should also reduce the efficiency of the slow beam-driven Langmuir waves decay, discussed hereafter.

4.2.2. Mutual Influence of Each Beam-Driven Langmuir Wave on the Decay of the Other Langmuir Wave

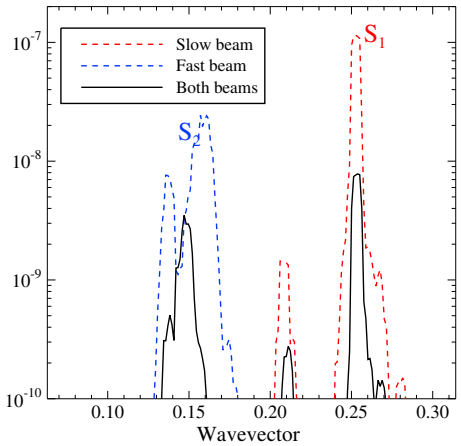

Figure 12. Comparison of the density fluctuation spectra showing the level of generated ion acoustic waves at time $\omega_{pe}t = 1.5 \times 10^4$ when the slow beam only (in dashed red), the fast beam only (in dashed blue), or both beams (in full black) are considered.

First, the parametric decay instability is a *threshold* process that depends on the electric field amplitude of the mother Langmuir wave packets. Thus, even a small decrease of the Langmuir electric energy can be sufficient to make the decay inefficient locally, as soon as the Langmuir wave packets amplitude gets below the decay threshold.

Second, the parametric decay instability is a *coherent* process that requires the beating of the mother and daughter Langmuir waves electric field to be phase locked with the ion acoustic density fluctuations. Such phase locking is greatly eased if the electric spectrum does not exhibit signatures at wave numbers close to the mother Langmuir waves (as is the case with only one electron beam). However, with two simultaneous electron beams with similar growth rates, two beam-driven Langmuir waves are generated at different wave numbers and the coherence of each Langmuir wave decreases. This reduces the

efficiency of the Langmuir decay of both the slow and fast beam-driven Langmuir waves. The consequences on the development of ion acoustic density fluctuations can be seen in Figure 12 that represents the spectrum of ion density fluctuations at time $\omega_{pe}t = 1.5 \times 10^4$, showing that both ion acoustic waves associated to the slow and fast beam-driven Langmuir waves decay are decreased in the presence of the other beam.

To conclude, two effects are combined to explain the inhibition of radio emission in the presence of two electron beams : (i) the screening of the fast beam by the slow beam in phase space that reduces the level of fast beam-driven Langmuir waves and (ii) the decrease of Langmuir coherence that affects both the decay of the slow and fast beam-driven Langmuir waves.

5. Conclusions

Through the combined analysis of remote observations of type III electromagnetic emissions and in situ observations of Langmuir waves, both performed by STEREO, this study supports the fundamental role played by the Langmuir waves in the generation of type III radio emissions. In particular, the observations reported in this paper, together with numerical simulations, indicate that the level of radio emission strongly depends on the amplitude and coherence level of the beam-driven Langmuir waves.

The main goal of this paper was the investigation of the type III radio emission depletion as two type III electron beams cross. We show that the observed depletion of radio emissions is explained by a reduced level of beam-driven Langmuir waves and by the decrease of the Langmuir wave coherence as the two beams cross. In particular, (i) the presence of the slow beam screens the quasilinear relaxation of the fast beam, thus limiting the bump-on-tail instability by the fast beam to a smaller range of wave number, (ii) the presence of two sets of Langmuir waves associated to the decrease of the Langmuir waves coherence affects the efficiency of the Langmuir decay. This picture is confirmed by different series of simulations using various parameters. The resulting energy injected into the mother Langmuir waves as well as the energy converted in the daughter waves is thus lower, and, as a consequence, the intensity of the electromagnetic emission is reduced.

We emphasize that the explanation of the observed radio depletion is robust enough not to depend on the physical mechanism responsible for the conversion of Langmuir waves into type III radio emissions, as long as the level of radio emissions depends on the level of beam-driven Langmuir waves and its coherence.

The mechanism at the origin of the strongest solar radio emission, namely the type III bursts, is still puzzling in spite of numerous effort to understand them. Various mechanisms are considered to explain the origin of type III electromagnetic emissions. According to the nonlinear conversion of Langmuir waves, type III radio emissions are expected to result from the decay of Langmuir waves. Evidence for electrostatic parametric decay were provided by *Henri et al.* [2009]. Evidence of in situ observations of electrostatic parametric decay are also provided in this paper. Since the electrostatic, as well as the electromagnetic, Langmuir decays are both parametric instabilities, their efficiencies indeed depend on the amplitude of the beam-driven Langmuir waves. In presence of two beams, the electrostatic/electromagnetic Langmuir decay generates daughter waves with reduced energy, as it has been illustrated here in the case of the electrostatic decay.

One last point is still puzzling. On the one hand, the remote observations show that the emission is at the fundamental of the plasma frequency, thus privileging an electromagnetic decay (either through a direct decay toward an electromagnetic wave—equation (2) or through coalescence—equation (3)). On the other hand, the in situ electric waveforms are compatible with an electrostatic decay (equation (1)). The discrimination between these two mechanisms, as well as the ability to observe in situ the electromagnetic decay of Langmuir waves, should be tackled in the future.

Acknowledgments
The authors thank the referees for their very interesting remarks that help in improving the manuscript. We are also grateful to the entire STEREO team and specifically the STEREO/WAVES team. The STEREO/WAVES instrument was designed, built, and is operated by teams at Paris Observatory, the University of Minnesota, the University of California, and Goddard Space Flight Center with the support of NASA and the French Space Agency CNES. The data from IMPACT, PLASTIC, and SECCHI were obtained from the STEREO Sciences Web page: http://stereo-ssc.nascom.nasa.gov/data/ins_data/.

Yuming Wang thanks Dejin Wu and Peter Yoon for their assistance in evaluating this paper.

References

Bale, S. D., et al. (2008), The electric antennas for the STEREO/WAVES experiment, *Space Sci. Rev.*, *136*, 529–547, doi:10.1007/s11214-007-9251-x.

Bougeret, J. L., et al. (2008), S/WAVES: The radio and plasma wave investigation on the STEREO mission, *Space Sci. Rev.*, *136*, 487–528, doi:10.1007/s11214-007-9298-8.

Cairns, I. H. (1987a), Second harmonic plasma emission involving ion sound waves, *J. Plasma Phys.*, *38*, 179–198, doi:10.1017/S0022377800012502.

Cairns, I. H. (1987b), Fundamental plasma emission involving ion sound waves, *J. Plasma Phys.*, *38*, 169–178, doi:10.1017/S0022377800012496.

Cairns, I. H., and P. A. Robinson (1992), Theory for low-frequency modulated Langmuir wave packets, *Geophys. Res. Lett.*, *19*, 2187–2190, doi:10.1029/92GL02632.

Dulk, G. A., J. L. Steinberg, S. Hoang, and M. V. Goldman (1987), The speeds of electrons that excite solar radio bursts of type III, *Astron. Astrophys.*, *173*, 366–374.

Field, G. B. (1956), Radiation by plasma oscillations, *Astrophys. J.*, *124*, 555, doi:10.1086/146261.

Galvin, A. B., et al. (2008), The Plasma and Suprathermal Ion Composition (PLASTIC) investigation on the STEREO observatories, *Space Sci. Rev.*, *136*, 437–486, doi:10.1007/s11214-007-9296-x.

Henri, P., C. Briand, A. Mangeney, S. D. Bale, F. Califano, K. Goetz, and M. Kaiser (2009), Evidence for wave coupling in type III emissions, *J. Geophys. Res.*, *114*, A03103, doi:10.1029/2008JA013738.

Henri, P., F. Califano, C. Briand, and A. Mangeney (2010), Vlasov-Poisson simulations of electrostatic parametric instability for localized Langmuir wave packets in the solar wind, *J. Geophys. Res.*, *115*, 106–119, doi:10.1029/2009JA014969.

Henri, P., N. Meyer-Vernet, C. Briand, and S. Donato (2011), Observations of Langmuir ponderomotive effects using the Solar TErrestrial RElations Observatory spacecraft as a density probe, *Phys. Plasmas*, *18*(8), 082,308, doi:10.1063/1.3622667.

Hoang, S., G. A. Dulk, and Y. Leblanc (1994), Interplanetary type 3 radio bursts that approach the plasma frequency: Ulysses observations, *Astron. Astrophys.*, *289*, 957–971.

Hoang, S., C. Lacombe, R. J. MacDowall, and G. Thejappa (2007), Radio tracking of the interplanetary coronal mass ejection driven shock crossed by Ulysses on 10 May 2001, *J. Geophys. Res.*, *112*, A09102, doi:10.1029/2006JA011906.

Hospodarsky, G. B., and D. A. Gurnett (1995), Beat-type Langmuir wave emissions associated with a type III solar radio burst: Evidence of parametric decay, *Geophys. Res. Lett.*, *22*, 1161–1164, doi:10.1029/95GL00303.

Howard, R. A., et al. (2008), Sun Earth Connection Coronal and Heliospheric Investigation (SECCHI), *Space Sci. Rev.*, *136*, 67–115, doi:10.1007/s11214-008-9341-4.

Kim, E.-H., I. H. Cairns, and P. A. Robinson (2008), Mode conversion of Langmuir to electromagnetic waves at magnetic field-aligned density inhomogeneities: Simulations, theory, and applications to the solar wind and the corona, *Phys. Plasmas*, *15*(10), 102,110, doi:10.1063/1.2994719.

Luhmann, J. G., et al. (2008), STEREO IMPACT investigation goals, measurements, and data products overview, *Space Sci. Rev.*, *136*, 117–184, doi:10.1007/s11214-007-9170-x.

Mangeney, A., F. Califano, C. Cavazzoni, and P. Travnicek (2002), A numerical scheme for the integration of the Vlasov-Maxwell system of equations, *J. Comput. Phys.*, *179*, 495–538.

Schleyer, F., I. H. Cairns, and E.-H. Kim (2013), Linear mode conversion of Langmuir/z-mode waves to radiation: Scalings of conversion efficiencies and propagation angles with temperature and magnetic field orientation, *Phys. Plasmas*, *20*(3), 032,101, doi:10.1063/1.4793726.

Tautz, R. C., A. Shalchi, and A. Dosch (2011), Simulating heliospheric and solar particle diffusion using the Parker spiral geometry, *J. Geophys. Res.*, *116*, A02102, doi:10.1029/2010JA015936.

Yoon, P. H. (1995), Plasma emission by a nonlinear beam instability, *Phys. Plasmas*, *2*, 537–548, doi:10.1063/1.870979.